

HybridINR-PCGC: Hybrid Lossless Point Cloud Geometry Compression Bridging Pretrained Model and Implicit Neural Representation

Wenjie Huang¹ Qi Yang² Shuting Xia¹ He Huang¹ Zhu Li² Yiling Xu^{1†}

¹ Shanghai Jiao Tong University ² University of Missouri-Kansas City

¹{huangwenjie2023, xiashuting, huanghe0429, yl.xu}@sjtu.edu.cn , ²{qiyang, lizhu}@umkc.edu

Abstract

Learning-based point cloud compression presents superior performance to handcrafted codecs. However, pretrained-based methods, which are based on end-to-end training and expected to generalize to all the potential samples, suffer from training data dependency. Implicit neural representation (INR) based methods are distribution-agnostic and more robust, but they require time-consuming online training and suffer from the bitstream overhead from the overfitted model. To address these limitations, we propose HybridINR-PCGC, a novel hybrid framework that bridges the pretrained model and INR. Our framework retains distribution-agnostic properties while leveraging a pretrained network to accelerate convergence and reduce model overhead, which consists of two parts: the Pretrained Prior Network (PPN) and the Distribution Agnostic Refiner (DAR). We leverage the PPN, designed for fast inference and stable performance, to generate a robust prior for accelerating the DAR’s convergence. The DAR is decomposed into a base layer and an enhancement layer, and only the enhancement layer needed to be packed into the bitstream. Finally, we propose a supervised model compression module to further supervise and minimize the bitrate of the enhancement layer parameters. Based on experiment results, HybridINR-PCGC achieves a significantly improved compression rate and encoding efficiency. Specifically, our method achieves a Bpp reduction of approximately 20.43% compared to G-PCC on 8iVFB. In the challenging out-of-distribution scenario Cat1B, our method achieves a Bpp reduction of approximately 57.85% compared to UniPCGC. And our method exhibits a superior time-rate trade-off, achieving an average Bpp reduction of 15.193% relative to the LINR-PCGC on 8iVFB.

1. Introduction

With the development of 3D sensing technology and computational power, point clouds have become a core data for-

Process	Pretrained-based	INR-based	Hybrid (ours)	
Pretrain	Pretrain Model	—	Pretrain Model	Enhance Base
Overfit	—	Refine Model	Pretrain Model	Enhance Base
Test	Pretrain Model	Refine Model	Pretrain Model	Enhance Base

Figure 1. Principle comparison of Pretrained-based, INR-based, and our Hybrid approaches, highlighting the model components utilized during the Pretrain, Overfit, and Test phases.

mat for numerous critical applications, such as autonomous driving [34, 38], Virtual Reality (VR), Augmented Reality (AR), and digital twins [3, 17]. Their massive data volume, however, poses significant challenges for storage and transmission [3, 7, 17, 25, 34]. Efficient point cloud compression (PCC) is therefore imperative. In general, point clouds consist of geometry and attributes, with geometry information serving as the foundation of point cloud data [36], and lossless geometry compression is particularly crucial for applications that require the preservation of original data precision.

Current mainstream Point Cloud Geometry Compression (PCGC) methods can be divided into three categories. First, traditional methods, such as the MPEG G-PCC [4, 13, 27] and V-PCC [14, 19], are highly stable and interpretable. Their primary limitation is suboptimal compression efficiency, as they rely on manually designed models that cannot fully exploit complex spatial correlations [7, 11, 12, 16]. Second, pretrained-based methods leverage deep neural networks to achieve State-Of-The-Art (SOTA) compression performance on specific datasets [7, 17]. These methods exhibit strong predictive performance when applied to data with a distribution similar to the training data, while they

demonstrate significant performance degradation when applied to Out-Of-Distribution (OOD) data. The third category, Implicit Neural Representation (INR) based methods, emerged to solve this generalization problem. By overfitting a network to each data instance, they achieve stable, distribution-agnostic compression performance [6, 7, 10, 15, 17, 18, 23, 26]. This paradigm, however, introduces two severe drawbacks: 1) it has to capture prior context from scratch during the overfitting stage, which makes encoding time-consuming, and 2) the overfitted network, which belongs to part of the bitstream, sometimes constitutes a relatively large portion of bitstream.

There is a clear trade-off between pretrained and INR-based methods: pretrained methods are fast at inference but fail to generalize, while INR methods generalize well but have longer inference times. To address these limitations, we propose HybridINR-PCGC, a novel framework that bridges the pretrained model and INR. Our motivation is to simultaneously maintain the desired distribution-agnostic characteristics of INR while leveraging a prior from a pretrained model to accelerate the overfitting process, as depicted in Fig. 1. The proposed method splits the overfitted network into two parts: a pretrained network and a refiner network, in which the refiner network consists of a base layer and an enhancement layer. The overall training strategy is: 1) first, train the pretrained network with the training dataset; 2) subsequently, train the refiner network with the training dataset under the prior provided by the pretrained network to derive the parameters as the base layer; 3) next, for the target point clouds, we overfit the refiner network to obtain the enhancement layer: the final parameters of the refiner network are the sum of the base and enhancement layers; 4) finally, the target point cloud is compressed by the pretrained network and the refiner network. The bitstream consists of point cloud geometry information and enhancement layer parameters. The overfitting time only includes online training of the enhancement layer.

Specifically, in HybridINR-PCGC, we design a Pretrained Prior Network (PPN) as the pretrained network and a Distribution Agnostic Refiner (DAR) as the refiner network. PPN aims to provide a robust prior to accelerate the convergence of DAR and reduce the model parameters that must be transmitted. Although SOTA pretrained-based methods, such as SparsePCGC [30] or UniPCGC [32], can be directly used as the pretrained network, these models are relatively complex and result in slow inference speed. Therefore, we design a lightweight network to implement PPN with fast inference speed and stable performance across different data distributions. It uses a feature masking operation to progressively refine its prior by incorporating previous decoded information from the DAR operating in 8 iterative stages. The DAR is a lightweight refiner network that consumes the prior from PPN and uses

modules like Sparse Convolution and MLPs to refine the final occupancy prediction. Finally, we propose a Supervised Model Compression (SMC) module to supervise and minimize the bitrate allocated to the parameters of the enhancement layer, thereby further reducing the model overhead. Our main contributions to the HybridINR-PCGC framework are summarized as follows:

- We propose HybridINR-PCGC, a novel framework that bridges pretrained models and INR to simultaneously resolve data dependency and high encoding time.
- We design an efficient PPN for iterative 8-stage prior generation, a lightweight DAR, decomposed into a base and enhancement layer, that uses the prior for prediction, and a SMC to supervise the enhancement layer and minimize its parameter size.
- Experimental results demonstrate a significantly improved compression rate and substantial savings in encoding time compared to SOTA pretrained and INR-based methods like UniPCGC and LINR-PCGC.

2. Related Work

2.1. Pretrained-based Methods

Pretrained-based methods use deep neural networks to model complex spatial relationships. These methods generally fall into two main architectural categories: Voxel-based representations and Tree-based structures [35]. **Voxel-based representations** are often accelerated by sparse convolutions to handle the inherent sparsity of point cloud data. PCGCv2 [29] and SparsePCGC [30] introduced multiscale frameworks using sparse tensors. SparsePCGC, in particular, processes only the Most-Probable Positively-Occupied Voxels (MP-POV) using a SparseCNN-based Occupancy Probability Approximation (SOPA) model. Building on this, UniPCGC [32] and Unicorn [31] proposed versatile, unified models for diverse compression tasks within a single framework. UniPCGC, for example, introduced an Uneven 8-Stage Lossless Coder (UELCC) and a Variable Rate and Complexity Module (VRCM). Other notable works in this area have also explored multiscale deep context modeling [22], learned convolutional transforms [24], and various autoregressive models. **Tree-based structures**, such as octrees, are used to organize the data and model probabilities. OctSqueeze [16] was an early work in this direction. More recently, OctSqueeze [16] was an early work in this direction. More recently, methods have integrated attention mechanisms to capture long-range dependencies, with notable examples including OctAttention [11] and TopNet [34]. Other methods, such as EHEM [28], OctFormer [8], and ECM-OPCC [20], have also advanced the state of the art in tree-based compression. While these methods demonstrate the power of learning-based priors, their reliance on a fixed, pretrained model is also their fundamental limitation

[33].

2.2. INR-based Methods

To address the generalization flaw inherent in pretrained models, an alternative paradigm of Implicit Neural Representation (INR) based methods was introduced. This approach achieves distribution-agnostic compression by overfitting a compact, coordinate-based network to a single point cloud instance [6, 10, 23, 26]. The set of optimized network weights then forms the compressed representation. While this per-instance optimization strategy grants excellent generalization, it introduces two critical drawbacks that have hindered its practical adoption. First, the online overfitting process is computationally expensive and amounts to complete network training, resulting in prohibitively time-consuming encoding [33]. Second, the entire set of overfitted network parameters must be quantized and encoded into the bitstream, creating significant model overhead [17]. These challenges of high encoding time and model overhead have mainly limited the application of pure INR methods to lossy compression [15, 18].

Recent research has focused on mitigating these issues. LINR-PCGC [17] was the first to address this for lossless compression by proposing a Group of Point Cloud (GoPC) framework. This method amortizes the model overhead by overfitting and sharing a single lightweight network across a group of frames. Furthermore, it accelerates the slow online training by using the network from the previous GoPC as an effective initialization for the current one [17]. Other hybrid approaches have also emerged. AnyPcc [33], for example, proposed an Instance-Adaptive Fine-Tuning (IAFT) strategy, which synergizes explicit and implicit paradigms. Instead of training a network from scratch, IAFT rapidly fine-tunes only a small subset of a powerful pretrained model’s weights to adapt to OOD instances [33]. However, this adaptation is restricted to the final prediction heads to keep the transmitted model overhead manageable. Lacking a mechanism to compress these model parameters, the framework cannot afford deeper fine-tuning. This limited adaptation scope may reduce robustness against challenging OOD data, motivating our hybrid approach, which explicitly manages this trade-off. These works demonstrate a clear trend toward hybrid solutions that seek to combine the fast inference of pretrained models with the generalization capabilities of INR.

3. Preliminary

3.1. Group of Point Cloud (GoPC)

The point cloud sequence is defined as $S = \{x_1, \dots, x_t, \dots, x_m\}$, where m is the total number of frames. Each frame x_t at time index t is composed of $\{C_t, F_t\}$, representing the **coordinates of occupied points**

(C_t) and their associated **attributes** (F_t), respectively. Since the focus is on coordinate compression, F_t is initialized as an all-ones vector. The sequence S is then uniformly partitioned into multiple **Groups of Point Cloud (GoPCs)**, such that $G_r = \{x_{(r-1)T+1}, \dots, x_m\}$ represents the r -th GoPC, with T being the fixed length of each group. Point clouds within the same GoPC have no interdependent relationship and are only used to share the overfitting time and network parameters. Therefore, in the following part, we use x to simplify the expression of x_t .

3.2. Octree Bottom-Up construction

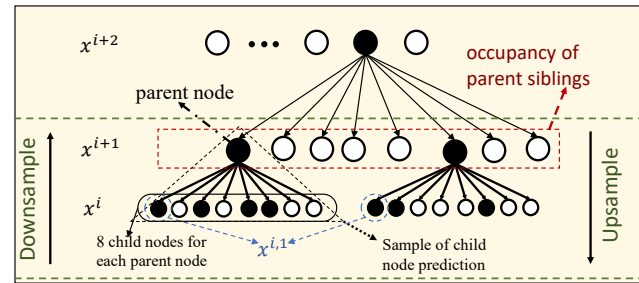


Figure 2. Concept in octree.

The Bottom-Up Octree construction shown in Fig. 2 is a core data structure for most point cloud coders. Each node is associated with a single-bit occupancy code, 0 for non-occupied and 1 for occupied. We call the octree levels as “spatial scales”, and Downsampling from a high scale x^i (child nodes) to a low scale x^{i+1} (parent nodes) is functionally equivalent to a Max Pooling operation with a 2^3 kernel. $x^{i,j}$ denotes the j -th child node of all nodes at scale i (e.g., the blue line in Fig. 2 represents all first child nodes, which are marked as $x^{i,1}$).

Most learning-based PCGC methods first apply this Downsampling process until a coarse representation at scale L . Their main contribution lies in the subsequent use of Upsampling that predicts the occupancy status of each child node from its parent nodes scale-by-scale. The predicted probabilities of child nodes from parent nodes are then leveraged by an arithmetic coder to encode/decode the actual occupancy. Finally, non-occupied nodes are pruned to generate a lossless reconstruction of higher scale.

The main task of our work is to improve the Upsampling operation for a better prediction of higher scale point clouds from lower scale point clouds to achieve better compression performance.

4. Method

4.1. Pipeline

The HybridINR-PCGC framework integrates a pretrained model with an INR to achieve efficient distribution-agnostic

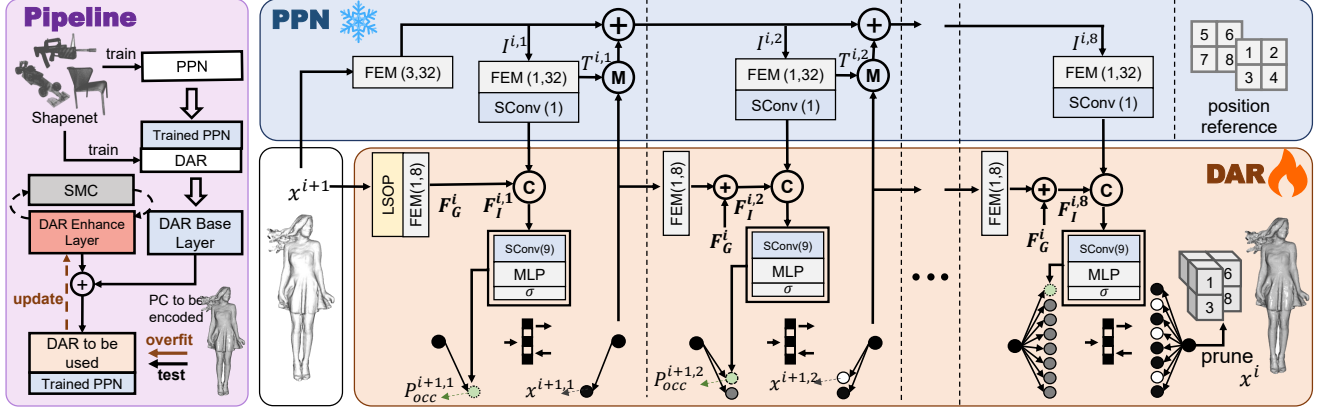


Figure 3. **Left:** The framework includes the Pipeline. **Top Right:** The architecture of the PPN, which iteratively generates a robust prior. **Bottom Right:** The architecture of the DAR, which consumes the prior from the PPN to refine the final occupancy prediction $F_{occ}^{i+1,j}$.

point cloud geometry compression. As shown in Fig. 3, the pipeline can be divided into four steps:

- Offline prior extraction. Use a large-scale training dataset (e.g. ShapeNet) to train the lightweight PPN, which supplies a robust prior.
- Base layer generation. Reuse the training dataset to train the DAR with prior from the frozen PPN. The resulting network parameters constitute the **base layer** of DAR, a high-quality initialization of DAR that accelerates subsequent online refinement.
- Instance-specific refinement. Initialize a group of learnable parameters with the same structure as DAR as the **enhancement layer** of DAR. Element-wise addition of the base and enhancement parameters yields the final DAR used in the framework. Keeping the PPN and base layer frozen, we overfit the enhancement layer on the target point cloud. Meanwhile, a SMC module is jointly optimized to balance enhancement parameter size and distortion.
- Compression. Entropy-code the geometry with prediction of DAR conditioned on PPN, and the quantized model parameters of DAR enhancement layer are included in the bitstream.

4.2. Pretrained Prior Network (PPN)

The PPN depicted in Fig. 3 aims to provide a robust prior with fast inference speed, thus accelerating the convergence of the DAR and reducing the number of transmitted model parameters. The PPN is a lightweight network designed to address the slow inference speed and complex structure of SOTA pretrained methods. Since the parameters of PPN do not appear in the bitstream, we only need to balance feature extraction performance and inference speed.

The prior from PPN is divided into 8 stages. This interaction forms a core iterative loop for each stage, indexed by $j = 1, 2, \dots, 8$: when decoding the j -th stage, PPN first generates a prior probability $P_{occ}^{i+1,j}$ based on available infor-

mation and provides it to DAR. DAR utilizes this prior to decode the child node occupancy $x^{i,j}$ for the current stage. Crucially, DAR then feeds the newly decoded child node occupancy result $x^{i,j}$ back to PPN, which uses it as updated information. The key effect of this 8-stage interaction is that the prior is progressively refined, as PPN continuously incorporates the newly decoded occupancy information from DAR to generate a more accurate prediction for the next stage, until all child nodes at the current scale are decoded. The detail of the collaboration of PPN and DAR is shown in Appendix Sec. 1.4.

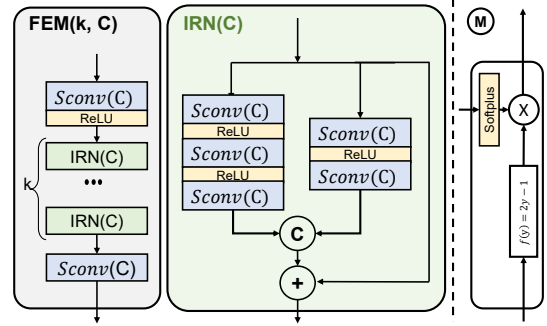


Figure 4. Component of PPN. **Left:** FEM and IRN. FEM(k, C) denotes FEM with k IRN Module and C hidden channel. **Right:** Processing of Feature Masking.

The input of PPN contains two parts: 1) global input: the low-scale point cloud x^{i+1} , and 2) stage input: the occupancy of the child nodes $x^{i,j}$ returned by DAR after PPN supplies prior of j -th stage. Eq. (1) shows the process of PPN,

$$\begin{aligned}
 I^{i,j} &= \begin{cases} FEM(x^{i+1}), & j = 1 \\ I^{i,j-1} + M(T^{i,j-1}, x^{i,j-1}), & j > 1 \end{cases} \\
 T^{i,j} &= FEM(I^{i,j}), \\
 M(u, v) &= \text{Softplus}(u) \cdot (2v - 1), \quad (1)
 \end{aligned}$$

the Feature Extraction Module (FEM) depicted on the left side of Fig. 4 is a block used to extract features. $SConv(\cdot)$ and $IRN(\cdot)$ denote Sparse Convolution and Inception Residual Network (IRN). $I^{i,j}$ is the input feature of each stage. $T^{i,j}$ is used to generate the prior and serve as the context information for the next stage. $M(\cdot)$ mainly uses the decoded occupancy of the child node to update the features calculated in the previous stage. Finally, we can calculate the prior information for DAR from $T^{i,j}$,

$$Pr^{i,j} = SConv(T^{i,j}). \quad (2)$$

4.3. Distribution Agnostic Refiner (DAR)

DAR depicted in Fig. 3 is designed to enforce the distribution-agnostic property by performing online overfitting while simultaneously ensuring rapid convergence and reducing parameter bitrate. This is achieved through a refining mechanism that builds upon the prior from PPN.

While DAR also operates in 8 stages per scale, its internal feature propagation method is deliberately different from PPN. Unlike PPN’s deep recurrent masking chain, DAR re-extracts features at each stage j from the set of all previously decoded child nodes ($x^{i,<j}$) using a FEM module. This design avoids a long gradient chain, which can accelerate the backpropagation speed during the online overfitting process. The input data of DAR contains two parts: 1) glob input: low-scale point cloud x^{i+1} . 2) stage input: decoded occupancy of the child node occupancy $x^{i,j-1}$ and the prior $Pr^{i,j}$ derived from PPN,

$$\begin{aligned} F_G^i &= FEM(LSOP(x^{i+1})), \\ F_I^{i,j} &= \begin{cases} F_G^i, & j = 1 \\ F_G^i + FEM(x^{i,<j}), & j > 1 \end{cases} \\ x^{i,<j} &= x^{i,1} \textcircled{C} x^{i,2} \textcircled{C} \dots \textcircled{C} x^{i,j-1}, \end{aligned} \quad (3)$$

Low Scale Occupancy Prior (LSOP) is a non-learning feature extraction module. It extracts the occupancy of the parent siblings as the condition feature to predict the occupancy of the child nodes. The siblings of the parent node are marked in red rectangles in Fig. 2. F_G^i represents the global features shared in all stages at scale i . $F_I^{i,j}$ is the feature of the input used for the prediction at each stage. When $j = 1$, F_G^i is used directly as $F_I^{i,1}$ since there is no previously decoded child node occupancy. \textcircled{C} represents channel concatenation. $x^{i,<j}$ indicates that the occupancies of the previously decoded child nodes are concatenated in the channel dimension. Subsequently, the $F_I^{i,j}$ is used to predict the probability of the child node occupancy in the current stage,

$$\begin{aligned} P_{occ}^{i,j} &= \sigma(MLP(SConv(F_I^{i,j} \textcircled{C} Pr^{i,j}))), \\ B^{i,j} &= Bce(x^{i,j}, P_{occ}^{i,j}), \\ Bce(u, v) &= u \log_2(v) + (1 - u) \log_2(1 - v), \end{aligned} \quad (4)$$

$MLP(\cdot)$ denotes MLP network, σ denotes ‘‘Sigmoid’’ that is used to apply normalization to the features to represent the occupancy probability. Bce is a binary cross-entropy used to estimate the bit rate of the current stage.

4.4. Supervised Model Compression (SMC)

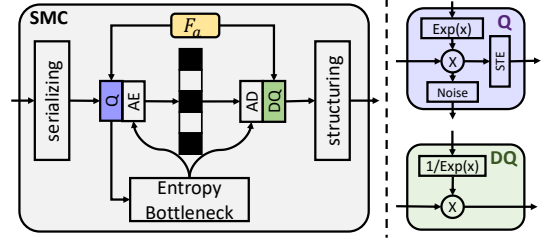


Figure 5. **Left:** Principle of SMC. **Right:** Quantization (Q) module and Dequantization (DQ) module in SMC. AE is an arithmetic encoder, AD is an arithmetic decoder.

The DAR enhancement layer parameters (p_m) are overfitted online and constitute the model overhead that must be included in the bitstream. There is a trade-off that a larger enhancement layer can improve prediction accuracy, while increasing the model bitrate. SMC module shown in Fig. 5 is specifically introduced to address this problem. By supervising and minimizing the bitrate allocated to these parameters, SMC ensures that the benefit of adaptation does not result in prohibitive model overhead. First, serialize the network parameters p_m into a vector v_m to facilitate subsequent processing,

$$v_m = serializing(p_m), \quad (5)$$

the subsequent process for v_m is divided into the reconstruction path and the bitstream estimation path. First, for the reconstruction path, the parameters v_m are hard-quantized to Q_m using straight-through estimator (STE) [2]. Q_m is then de-quantized to \hat{v}_m and restructured to \hat{p}_m , which are the parameters used in the network.

$$\begin{aligned} Q_m &= STE(e^{F_a} \cdot v_m), \\ \hat{v}_m &= Q_m / e^{F_a}, \\ \hat{p}_m &= structuring(\hat{v}_m), \end{aligned} \quad (6)$$

where F_a is a learnable parameter associated with quantization. Second, for the bitrate estimation path, \tilde{Q}_m is created as a continuous proxy by adding uniform noise $U(-0.5, 0.5)$ to v_m to estimate the bitrate differentially. $Entropy(\cdot)$ is the Entropy Bottleneck [1] used to model the probability distribution,

$$\begin{aligned} \tilde{Q}_m &= e^{F_a} \cdot v_m + U(-0.5, 0.5), \\ Prob_m &= Entropy(\tilde{Q}_m), \\ Bit_m &= - \sum \log_2(Prob_m), \end{aligned} \quad (7)$$

where \tilde{Q}_m is a differentiable quantification result of v_m . $Prob_m$ is the probability estimated by the Entropy Bottleneck. Bit_m is the estimated bitrate of p_m .

4.5. Loss Function

The total loss \mathcal{L} is designed to minimize the total estimated bitrate, which is expressed in bits per point (bpp). In our hybrid framework, the final bitstream consists of two distinct components: the child node occupancy of each scale, i.e., \mathcal{L}_{pred} , and the overfitted model parameters of the DAR enhancement layer, i.e., \mathcal{L}_{model} ,

$$\begin{aligned} \mathcal{L} &= \mathcal{L}_{pred} + \mathcal{L}_{model}, \\ \mathcal{L}_{pred} &= \frac{\sum_i \sum_j B^{i,j}}{N}, \mathcal{L}_{model} = \frac{Bit_m}{N \cdot T}, \end{aligned} \quad (8)$$

where $B^{i,j}$ is the estimated bitrate for the j -th stage at spatial scale i , and N is the number of points in the input point cloud. Bit_m is the estimated bitrate of the DAR enhancement layer parameters p_m , and T is the size of the GoPC.

5. Experiment

5.1. Experiment Configuration

Datasets. The pretrained part of our model is trained using the large-scale **ShapeNet** [5] dataset. For performance evaluation, we test our method on four standard public datasets. For dynamic sequences, we use 8i Voxelized Full Bodies (**8iVFB**) [9], OwlII Dynamic Human DPC (**OwlII**) [37], Microsoft Voxelized Upper Bodies (**MVUB**) [21], which mainly consist of various point clouds of different characters. We also include static objects from the **PCRM Cat1B** (marked as Cat1B) dataset (CandleStick13, Clock13, Bicycle13) to demonstrate performance in a broader range of content. These datasets also allow us to test generalization across different data distributions. The geometric distributions of **8iVFB** and **OwlII** show high consistency with ShapeNet. **MVUB** presents some geometric distribution differences, featuring fragmented parts and non-smooth surfaces. **Cat1B** exhibits a very large geometric distribution difference from ShapeNet, characterized by high quantization precision and highly irregular point arrangements. An overview of the testing datasets is provided in Fig. 7.

Baselines. We compare our proposed HybridINR-PCGC (marked as Hybrid) against several SOTA methods. For traditional codecs, we use the MPEG standard **G-PCC** (TMC13v23) [13] as an anchor. For pretrained-based methods, we provide a comprehensive comparison against the leading frameworks: the lossless configurations of **SparsePCGC** [29] (marked as S.PCGC) and **UniPCGC** [32]. To ensure a fair comparison, both pretrained baselines are trained on the **ShapeNet** dataset. For the INR-based methods, we use **LINR-PCGC** [17] (marked as LINR.) as the representation. For both LINR-PCGC and our method,

we have disabled the initialization strategy [17], which impairs encoding parallelism across GoPCs.

Implementation Details. All training and testing experiments are conducted on a single NVIDIA RTX 3090 GPU. Further details on all hyperparameters, such as learning rates, optimizer settings, and specific parameter values, are provided in the Appendix. For 8iVFB, OwlII, and MVUB, we set the GoPC size to 32 frames and test 96 frames per sequence. For the static sequences in PCRM Cat1B, as a single frame in PCRM Cat1B already contains tens of millions of points, we first partition each object into sub-frames of approximately 200,000 points using K-D tree. These sub-frames are then treated as sequential “frames” for compression.

Evaluation Metrics. We evaluate performance using three primary metrics: bitrate measured in Bits per point (Bpp), and the Encoding/Decoding (Enc/Dec) Time in seconds (s). To evaluate the trade-off between Enc Time and Bpp, we also analyze the *Time-Bpp Performance*, which plots Bpp (y-axis) against the Enc Time (x-axis) call Time-Bpp curve. To quantitatively compare the overall compression efficiency over time, we propose the **Time-Bpp Rate (TB-Rate)** metric, which measures the average Bpp reduction of one method relative to another: given two Time-Bpp curves $R_A(t)$ and $R_B(t)$:

$$\text{TB-Rate} = \left(\frac{\int_{t_{\min}}^{t_{\max}} R_A(t) dt}{\int_{t_{\min}}^{t_{\max}} R_B(t) dt} - 1 \right) \times 100\%.$$

Here, $[t_{\min}, t_{\max}]$ denotes the overlapping Enc Time range between the two methods. t_{\max} is typically set as the convergence decision point of the slower of the two methods. A negative TB-Rate indicates that method A achieves a lower Bpp than method B on average.

5.2. Experiment Result

Fig. 6 presents the average Time-Rate curves for all four test datasets. We see that HybridINR-PCGC is consistently positioned in the bottom-left, demonstrating a superior time-rate trade-off compared to all baselines (G-PCC, SparsePCGC, UniPCGC, and LINR-PCGC). This figure highlights two key findings related to data distribution. First, for datasets with distributions similar to the training data, such as 8iVFB and OwlII, HybridINR-PCGC shows extremely fast convergence. It achieves a superior Bpp and surpasses all baseline methods (traditional, pretrained, and INR-based) within a very short encoding time. Second, as the data distribution gap of the target sample with the training data increases, the performance of pretrained methods (SparsePCGC, UniPCGC) degrades significantly. In contrast, HybridINR-PCGC remains robust. It achieves a competitive compression rate within a reasonable time, and as overfitting progresses, it continues to converge toward

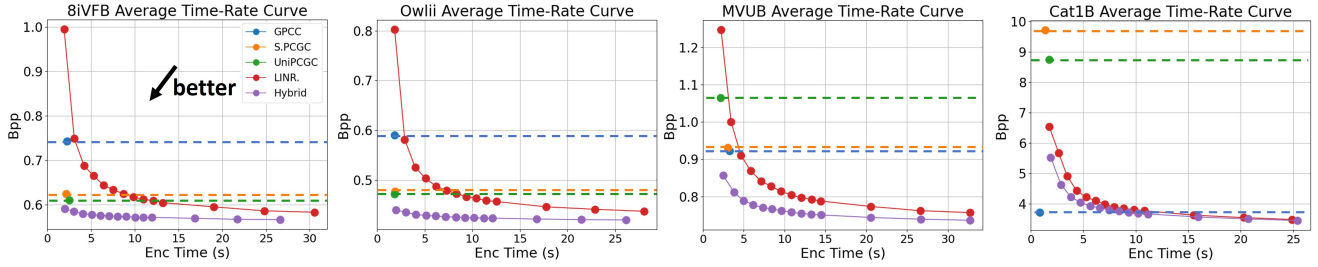


Figure 6. Enc Times vs. Bpp comparison of different methods. The Enc Time of HybridINR-PCGC contains the prior extracting time in PPN and the overfitting time of DAR enhancement layer.

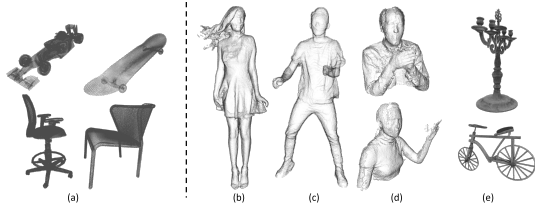


Figure 7. Dataset exhibition. (a) Sample of ShapeNet. (b) RedandBlack in 8iVFB. (c) Dancer in OwlII. (d) Phil10 (up) and Sarah10 (down) in MVUB. (e) CandleStick13 (up) and Bicycle13 (down) in Cat1B.

the best overall compression performance, demonstrating strong generalization ability.

We sample two rate points to construct Tab. 1 and Tab. 2, in which “ours” represents a point where our method is approaching convergence, “ours2” denotes a point of full convergence after extended overfitting time. According to the quantitative results, we can observe that: 1) when operating at a comparable encoding time, our method achieves the best compression. For example, on 8iVFB, “ours” achieves 0.592 Bpp in 2.026s, outperforming SparsePCGC (0.625 Bpp in 2.159s) and UniPCGC (0.611 Bpp in 2.506s); 2) with extended encoding time, our method can achieve even higher compression ratios, such as 0.567 Bpp on 8iVFB.

To quantitatively summarize the entire Time-Rate curve, we report the TB-Rate metric, setting LINR-PCGC as the anchor, and the results are shown in Tab. 3. We see that our method achieves significant gains, with an average Bpp reduction of -15.193% on 8iVFB, -16.953% on OwlII, -12.1% on MVUB, and -7.422% on Cat1B. Besides, Tab. 4 illustrates the decoding time. Our method (“ours”) demonstrates efficient decoding performance, proving significantly faster than UniPCGC across all datasets (e.g., 0.941s vs. 1.458s on OwlII) and maintaining speeds comparable to G-PCC and SparsePCGC.

5.3. Network Parameter Distribution Analysis

To validate the effectiveness of SMC, we analyze its supervision of the DAR enhancement layer parameters in

	G-PCC	S.PCGC	UniPCGC	ours	ours2
8iVFB	0.744	0.625	0.611	0.592	0.567
OwlII	0.59	0.477	0.472	0.44	0.42
MVUB	0.922	0.931	1.064	0.812	0.736
Cat1B	3.711	9.71	8.747	3.687	3.446

Table 1. Quantitative results of Bpp on different dataset.

	G-PCC	S.PCGC	UniPCGC	ours	ours2
8iVFB	2.265	2.159	2.506	2.026	26.616
OwlII	1.857	1.902	1.841	1.995	26.148
MVUB	3.277	3.06	2.161	3.805	32.737
Cat1B	0.843	1.37	1.742	10.244	25.415

Table 2. Quantitative results of Enc Time on different dataset.

	8iVFB	OwlII	MVUB	Cat1B
	-15.193	-16.953	-12.1	-7.422

Table 3. TB-Rate(%) comparison over LINR-PCGC.

	G-PCC	S.PCGC	UniPCGC	LINR.	ours
8iVFB	0.859	1.03	2.063	0.841	0.964
OwlII	0.676	0.91	1.458	0.781	0.941
MVUB	1.198	1.461	1.719	0.907	1.242
Cat1B	0.496	0.639	1.333	0.755	0.902

Table 4. Quantitative results of Dec Time on different dataset.

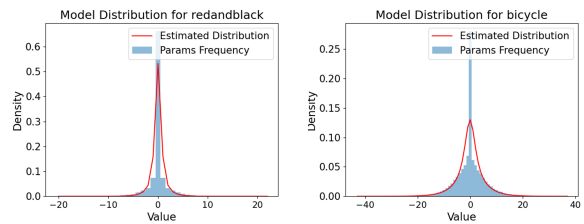


Figure 8. Parameter distribution of enhancement layer of DAR.

	Bpp(%)	Enc(%)	Dec(%)
overfit	-	68.77	-
prior	-	11.08	35.05
scale2~8	5.57	9.32	28.99
scale1	17.49	3.34	10.84
scale0	76.08	7.45	25.04
model	0.85	0.04	0.09

Table 5. Statistics of bitstream proportion and Enc/Dec Time proportion (%) in MVUB.

Fig. 8. We use RedandBlack from 8iVFB and Bicycle13 from Cat1B as examples: the blue bars show the frequency of parameters and their widths represent the learned quantization step size. This visualization highlights two key functions of the SMC. First, it balances the fitting ability and bitrate by learning an optimal quantization precision for different parameter values. The quantization step size for the samples, which geometry distribution is similar to the training dataset, is larger, while the quantization step size for geometry distribution that diverges from the training dataset is smaller. Second, the red curve, which represents the estimated probability from the Entropy Bottleneck, accurately matches the actual parameter frequency. This accurate estimation is crucial for efficient entropy coding, as it allows the arithmetic coder to minimize the final parameter bitrate.

5.4. Bpp Allocation and Time Composition

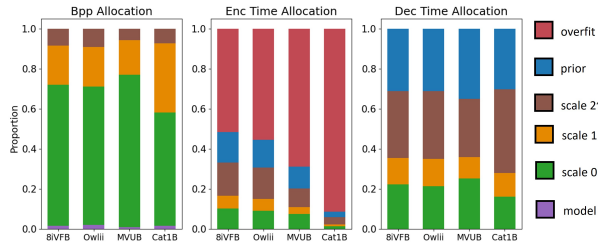


Figure 9. Bitstream allocation and time composition.

We analyze the bitstream allocation and time composition of “ours” configuration (reported in Tab. 1) in Sec. 5.2, with a visual overview in Fig. 9 and specific statistics for MVUB in Tab. 5. Geometry occupancy dominates the bitstream size and progressively decrease with scale: scale 0 consumes 76.08% of the total bitrate, whereas the cumulative share for scales 2 to 8 drops to 5.57%. The model parameter size is minimal at only 0.85%. Enc Time is dominated by the instance-specific refinement, with the “overfit” step alone accounting for 68.77% of the total Enc Time. Dec Time is distributed differently: a significant portion is consumed by the prior extraction (35.05%).

	8iVFB	OwlII	MVUB	Cat1B
w.o. SMC	3.35	3.54	8.23	1.99
w.o. SMC&PPN	17.98	17.94	8.82	11.36

Table 6. TB-Rate (%) with respect to the full HybridINR-PCGC model.

5.5. Ablation Study

To demonstrate the effectiveness of each module, we conduct ablation studies on two key components: the PPN and the SMC module. We use the TB-Rate metric against the full HybridINR-PCGC model, where positive values indicate performance loss. Fig. 10 provides the Time-Bpp curves, while Tab. 6 quantifies the results. Removing only the SMC module (“w.o. SMC”) results in a consistent performance loss, e.g., 3.35% on 8iVFB and 1.99% on Cat1B, which confirms that SMC is critical for reducing model parameters overhead. Removing both SMC and the PPN prior (“w.o. SMC&PPN”) causes a further degradation, e.g., 17.98% on 8iVFB and 11.36% on Cat1B. This large loss underscores the PPN’s critical role in accelerating convergence, validating our hybrid approach.

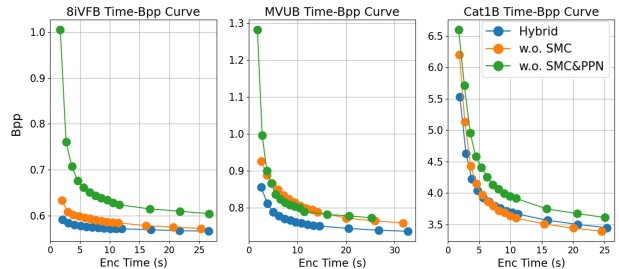


Figure 10. Impact of each module in HybridINR-PCGC.

5.6. Conclusion

In this paper, we propose HybridINR-PCGC, a novel hybrid framework that successfully bridges pretrained models and INR for efficient, distribution-agnostic point cloud compression. By leveraging a PPN to accelerate the convergence lightweight DAR and using a SMC module to minimize model overhead, our method achieves SOTA compression ratio and TB-Rate performance. Experiments show that our framework significantly outperforms existing methods and, crucially, demonstrates strong generalization to OOD data where pretrained methods falter.

References

- [1] Johannes Ballé, David Minnen, Saurabh Singh, Sung Jin Hwang, and Nick Johnston. Variational image compression with a scale hyperprior. 2018. 5

- [2] Yoshua Bengio, Nicholas Léonard, and Aaron Courville. Estimating or propagating gradients through stochastic neurons. *arXiv preprint arXiv:1308.3432*, 2013. 5
- [3] C. Cao, M. Preda, and T. Zaharia. 3D point cloud compression: A survey. In *Proceedings of the 24th International Conference on 3D Web Technology*, 2019. 1
- [4] Chao Cao, Marius Preda, Vladyslav Zakharchenko, Euee S Jang, and Titus Zaharia. Compression of sparse and dense dynamic point clouds—methods and standards. *Proceedings of the IEEE*, 109(9):1537–1558, 2021. 1
- [5] A. X. Chang, T. Funkhouser, L. Guibas, P. Hanrahan, et al. Shapenet: An information-rich 3d model repository. *ArXiv*, abs/1512.03012, 2015. 6
- [6] Hao Chen, Bo He, Hanyu Wang, Yixuan Ren, Ser Nam Lim, and Abhinav Shrivastava. Nerv: Neural representations for videos. *Advances in Neural Information Processing Systems*, 34:21557–21568, 2021. 2, 3
- [7] C. Choy, J. Gwak, and S. Savarese. 4D spatio-temporal convnets: Minkowski convolutional neural networks. In *Proceedings of the IEEE/CVF Conference on Computer Vision and Pattern Recognition*, pages 3075–3084, 2019. 1, 2
- [8] Mingyue Cui, Junhua Long, Mingjian Feng, Boyang Li, and Kai Huang. Octformer: Efficient octree-based transformer for point cloud compression with local enhancement. In *Proceedings of the AAAI Conference on Artificial Intelligence*, pages 470–478, 2023. 2
- [9] Eugene d’Eon, Bob Harrison, Taos Myers, and Philip A. Chou. 8i voxelized full bodies: a voxelized point cloud dataset. ISO/IEC JTC1/SC29 Joint WG11/WG1 (MPEG/JPEG) input document m40059/M74006, 2017. 6
- [10] Emilien Dupont, Adam Goliński, Milad Alizadeh, Yee Whye Teh, and Arnaud Doucet. COIN: COmpression with Implicit Neural Representations. 2021. 2, 3
- [11] C. Fu, G. Li, R. Song, W. Gao, and S. Liu. OctAttention: Octree-based large-scale contexts model for point cloud compression. In *Proceedings of the AAAI Conference on Artificial Intelligence*, pages 625–633, 2022. 1, 2
- [12] D. Graziosi, O. Nakagami, S. Kuma, A. Zaghetto, T. Suzuki, and A. Tabatabai. An overview of ongoing point cloud compression standardization activities: Video-based (V-PCC) and geometry-based (G-PCC). *APSIPA Transactions on Signal and Information Processing*, 2020. 1
- [13] MPEG Group. Mpeg-pcc-tmc13. <https://github.com/MPEGGroup/mpeg-pcc-tmc13/releases/tag/release-v23.0-rc2>, . Accessed: 2024-09-10. 1, 6
- [14] MPEG Group. Mpeg-pcc-tmc2. <https://github.com/MPEGGroup/mpeg-pcc-tmc2/releases/tag/release-v23.0>, . Accessed: 2024-09-10. 1
- [15] Yueyu Hu and Yao Wang. Learning neural volumetric field for point cloud geometry compression. In *Proceedings of the 2022 Picture Coding Symposium*, pages 127–131, 2022. 2, 3
- [16] L. Huang, S. Wang, K. Wong, J. Liu, and R. Urtasun. OctSqueeze: Octree-structured entropy model for LiDAR compression. In *Proceedings of the IEEE/CVF Conference on Computer Vision and Pattern Recognition*, pages 1310–1320, 2020. 1, 2
- [17] Wenjie Huang, Qi Yang, Shuting Xia, He Huang, Yiling Xu, and Zhu Li. Linr-pcgc: Lossless implicit neural representations for point cloud geometry compression. pages 28577–28586, 2025. 1, 2, 3, 6
- [18] Berivan Isik, Philip A Chou, Sung Jin Hwang, Nick Johnston, and George Toderici. Lvac: Learned volumetric attribute compression for point clouds using coordinate based networks. *Frontiers in Signal Processing*, 2:1008812, 2022. 2, 3
- [19] Euee S. Jang, Marius Preda, Khaled Mammou, Alexis M. Tourapis, Jungsun Kim, Danilo B. Graziosi, Sungryeul Rhyu, and Madhukar Budagavi. Video-based point-cloud-compression standard in mpeg: From evidence collection to committee draft [standards in a nutshell]. *IEEE Signal Processing Magazine*, 36(3):118–123, 2019. 1
- [20] Yiqi Jin, Ziyu Zhu, Tongda Xu, Yuhuan Lin, and Yan Wang. ECM-OPCC: Efficient context model for octree-based point cloud compression. In *ICASSP 2024 - 2024 IEEE International Conference on Acoustics, Speech and Signal Processing (ICASSP)*, pages 7985–7989, 2024. 2
- [21] Charles Loop, Qin Cai, Sergio Orts Escolano, and Philip A. Chou. Microsoft voxelized upper bodies a voxelized point cloud dataset. ISO/IEC JTC1/SC29 Joint WG11/WG1 (MPEG/JPEG) input document m38673/M72012, 2016. 6
- [22] D. T. Nguyen, M. Quach, G. Valenzise, and P. Duhamel. Multiscale deep context modeling for lossless point cloud geometry compression. In *Proceedings of the IEEE International Conference on Multimedia and Expo Workshops*, 2021. 2
- [23] Francesca Pistilli, Diego Valsesia, Giulia Fracastoro, and Enrico Magli. Signal compression via neural implicit representations. In *Proceedings of the 2022 IEEE International Conference on Acoustics, Speech, and Signal Processing*, pages 3733–3737, 2022. 2, 3
- [24] M. Quach, G. Valenzise, and F. Dufaux. Learning convolutional transforms for lossy point cloud geometry compression. In *Proceedings of the IEEE International Conference on Image Processing*, pages 4320–4324, 2019. 2
- [25] M. Quach, J. Pang, D. Tian, G. Valenzise, and F. Dufaux. Survey on deep learning-based point cloud compression. *Frontiers in Signal Processing*, 2022. 1
- [26] Hongning Ruan, Yulin Shao, Qianqian Yang, Liang Zhao, and Dusit Niyato. Point cloud compression with implicit neural representations: A unified framework. In *Proceedings of the 2024 IEEE/CIC International Conference on Communications in China*, pages 1709–1714, 2024. 2, 3
- [27] S. Schwarz, M. Preda, V. Baroncini, et al. Emerging MPEG standards for point cloud compression. *IEEE Journal on Emerging and Selected Topics in Circuits and Systems*, 2018. 1
- [28] Rui Song, Chunyang Fu, Shan Liu, and Ge Li. Efficient hierarchical entropy model for learned point cloud compression. In *Proceedings of the IEEE/CVF Conference on Computer Vision and Pattern Recognition*, pages 14368–14377, 2023. 2
- [29] J. Wang, D. Ding, Z. Li, and Z. Ma. Multiscale point cloud geometry compression. In *Proceedings of the Data Compression Conference*, pages 73–82, 2021. 2, 6

- [30] J. Wang, D. Ding, Z. Li, X. Feng, C. Cao, and Z. Ma. Sparse tensor-based multiscale representation for point cloud geometry compression. *IEEE Transactions on Pattern Analysis and Machine Intelligence*, 45(7):9055–9071, 2023. [2](#)
- [31] J. Wang, R. Xue, J. Li, D. Ding, Y. Lin, and Z. Ma. A versatile point cloud compressor using universal multiscale conditional coding part I: Geometry. *IEEE Transactions on Pattern Analysis and Machine Intelligence*, 2025. [2](#)
- [32] Kangli Wang and Wei Gao. UniPCGC: Towards practical point cloud geometry compression via an efficient unified approach. In *Proceedings of the AAAI Conference on Artificial Intelligence*, pages 12721–12729, 2025. [2](#), [6](#)
- [33] Kangli Wang, Qianxi Yi, Yuqi Ye, Shihao Li, and Wei Gao. AnyPcc: Compressing any point cloud with a single universal model. *arXiv preprint arXiv:2510.20331*, 2025. [3](#)
- [34] Xinjie Wang, Yifan Zhang, Ting Liu, Xinpu Liu, Ke Xu, Jianwei Wan, Yulan Guo, and Hanyun Wang. TopNet: Transformer-efficient occupancy prediction network for octree-structured point cloud geometry compression. In *Proceedings of the IEEE/CVF Conference on Computer Vision and Pattern Recognition*, pages 27305–27314, 2025. [1](#), [2](#)
- [35] Yiling Xu, Yujie Zhang, Shuting Xia, Kaifa Yang, He Huang, Ziyu Shan, Wenjie Huang, Qi Yang, and Le Yang. Point cloud compression and objective quality assessment: A survey, 2025. [2](#)
- [36] Qi Yang, Zhan Ma, Yiling Xu, Zhu Li, and Jun Sun. Inferring point cloud quality via graph similarity. *IEEE Transactions on Pattern Analysis and Machine Intelligence*, 44(6):3015–3029, 2022. [1](#)
- [37] X. Yi, L. Yao, and W. Ziyu. OwlII dynamic human mesh sequence dataset. ISO/IEC JTC1/SC29/WG11 (MPEG/JPEG) input document m41658, 2017. [6](#)
- [38] Kang You, Tong Chen, Dandan Ding, M Salman Asif, and Zhan Ma. Reno: Real-time neural compression for 3d lidar point clouds. pages 22172–22181, 2025. [1](#)

HybridINR-PCGC: Hybrid Lossless Point Cloud Geometry Compression Bridging Pretrained Model and Implicit Neural Representation

Supplementary Material

1. Appendix

1.1. Detail of parameters

The details of the parameters in our experiment are listed in Tab. 7.

Symbol	Description	Value
GoPC	The group size of point cloud	32
lr_o	Learning rate when overfitting	0.01
$epoch_o$	Set the upper limit of epochs for overfitting	26
γ_o	Multiplicative factor of learning rate decay in StepLR when overfitting	0.0001
lr_o^{min}	The minimum value of the learning rate when overfitting	0.0004
lr_p	Learning rate when pretraining	0.008
$epoch_p$	Set the upper limit of epochs for pretraining	25
γ_p	Multiplicative factor of learning rate decay in StepLR when pretraining	0.0001
lr_p^{min}	The minimum value of the learning rate when pretraining	0.0004

Table 7. Detail of parameters of our experiment.

1.2. Supplementary Experiment result

Supplementary results of the main experiment. In the main experiment result Sec. 5.2, we demonstrate the average Bpp of a whole dataset. In this section, we present the Bpp of all sequences for each dataset. We calculate the average result of Bpp, Enc/Dec Time for each dataset. The results are shown in Tabs. 8 to 11. From the tables, we can observe that HybridINR-PCGC still obtains the best compression performance on all sequences of each dataset.

Supplementary result of the analysis of the distribution of network parameters. In Sec. 5.3, we demonstrate the comparison between RedandBlack from 8iVFB and bicycle13 from Cat1B. Here, we sample a sequence from each dataset to show the estimation of network parameters distribution and the adaptive quantization step in SMC. From Fig. 11, we can observe that the larger the geometric distribution gap, the smaller the quantization step to be used. The distribution estimation will also change along with the variation of the network parameter distribution.

	GPCC	S.PCGC	UniPCGC	ours	ours2
Longdress	0.741	0.619	0.603	0.587	0.563
Loot	0.69	0.586	0.565	0.551	0.528
Red&Black	0.81	0.676	0.669	0.652	0.627
Soldier	0.734	0.619	0.606	0.577	0.549
Bpp (avg)	0.744	0.625	0.611	0.592	0.567
Enc Time	2.265	2.159	2.506	2.026	26.616
Dec Time	0.859	1.03	2.063	0.964	0.921

Table 8. Detail result of 8iVFB. The abbreviations in the table are the same as the settings in the main experiment.

	GPCC	S.PCGC	UniPCGC	ours	ours2
Basketball	0.578	0.466	0.457	0.427	0.409
Dancer	0.606	0.485	0.478	0.448	0.428
Exercise	0.585	0.472	0.465	0.435	0.414
Model	0.593	0.485	0.488	0.452	0.429
Bpp (avg)	0.59	0.477	0.472	0.44	0.42
Enc Time	1.857	1.902	1.841	1.995	26.148
Dec Time	0.676	0.91	1.458	0.941	0.893

Table 9. Detail result of OwlII

	GPCC	S.PCGC	UniPCGC	ours	ours2
Andrew10	0.941	0.947	1.071	0.835	0.764
David10	0.898	0.909	1.036	0.789	0.712
Phil10	0.969	0.966	1.103	0.844	0.769
Ricardo10	0.909	0.929	1.085	0.802	0.719
Sarah10	0.894	0.903	1.026	0.788	0.718
Bpp (avg)	0.922	0.931	1.064	0.812	0.736
Enc Time	3.277	3.06	2.161	3.805	32.737
Dec Time	1.198	1.461	1.719	1.242	1.221

Table 10. Detail result of MVUB

Additional results regarding bitstream allocation and time composition. In the Sec. 5.4, we demonstrate the detailed table on bitstream allocation and time composition in MVUB. Here, we supply more results in Tabs. 12 to 14 for other test data, including 8iVFB, OwlII and Cat1B.

Additional figure for the ablation study. In the ablation study Sec. 5.5, due to space limitations, we omit the results on the OwlII platform. The results on OwlII are presented in Fig. 12.

	GPCC	S.PCGC	UniPCGC	ours	ours2
Bicycle13	3.252	8.916	7.952	3.116	2.923
CandleStick13	3.705	9.791	8.922	3.586	3.326
Clock13	4.175	10.422	9.367	4.36	4.089
Bpp (avg)	3.711	9.71	8.747	3.687	3.446
Enc Time	0.843	1.37	1.742	10.244	25.415
Dec Time	0.496	0.639	1.333	0.902	0.911

Table 11. Detail result of Cat1B

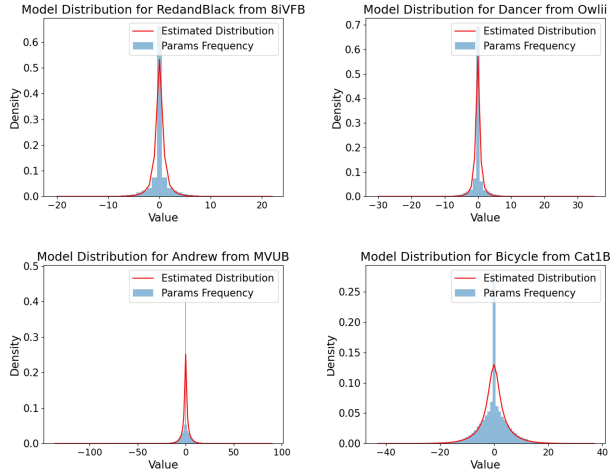


Figure 11. Completed comparison of model parameter distribution

	Bpp(%)	Enc(%)	Dec(%)
overfit	-	51.54	-
prior	-	15.3	31.07
scale2~8	8.5	16.48	33.37
scale1	19.43	6.36	13.21
scale0	70.55	10.28	22.28
model	1.52	0.04	0.07

Table 12. Statistics of bitstream proportion and Enc/Dec Time proportion (%) in 8iVFB.

	Bpp(%)	Enc(%)	Dec(%)
overfit	-	55.34	-
prior	-	14.02	31.21
scale2~8	9.1	15.72	33.8
scale1	19.78	5.83	13.67
scale0	68.97	8.99	21.2
model	2.15	0.09	0.11

Table 13. Statistics of bitstream proportion and Enc/Dec Time proportion (%) in OwlII.

	Bpp(%)	Enc(%)	Dec(%)
overfit	-	91.4	-
prior	-	2.62	30.33
scale2~8	7.32	3.6	41.65
scale1	34.46	1.0	11.77
scale0	56.65	1.35	16.13
model	1.58	0.02	0.11

Table 14. Statistics of bitstream proportion and Enc/Dec Time proportion (%) in Cat1B.

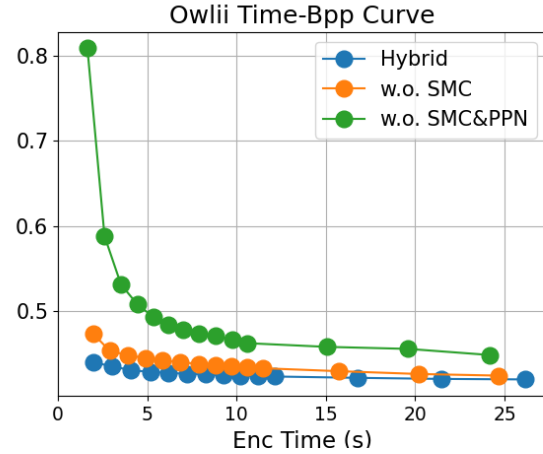


Figure 12. The ablation result on OwlII

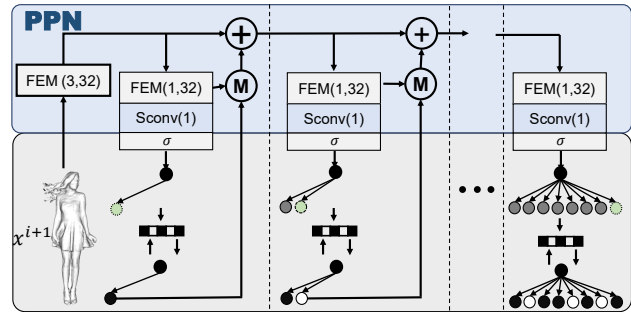


Figure 13. Details of the PPN training process.

1.3. More Detail About PPN

The pretraining detail of PPN. PPN is designed to function iteratively by receiving decoded child node occupancy feedback from the DAR in the main framework. However, PPN must first be trained independently on a large-scale dataset (e.g., ShapeNet). To define how PPN is pre-trained when separated from DAR, we treat PPN as a standalone prediction network. The process of obtaining the prior feature $P_r^{i,j}$ is identical to its operation within the hybrid framework, the feature $P_r^{i,j}$ is directly converted into an occupancy probability value $P_o^{i,j}$ using the Sigmoid

Algorithm 1: Collaborative prediction of PPN and DAR

Input: Low scale point cloud x^{i+1} , PPN and DAR parameters.

Output: Predicted probabilities $\mathcal{P} = \{P_{occ}^{i,j}\}_{j=1}^8$.

- 1 Initialize decoded child nodes $x^{i,<1} \leftarrow \emptyset$ and probability set $\mathcal{P} \leftarrow \emptyset$;
- 2 Extract global feature F_G^i for DAR from the low scale input (Eq. 3);
- 3 $F_G^i \leftarrow \text{FEM}(\text{LSOP}(x^{i+1}))$;
- 4 **for** $j \leftarrow 1$ **to** 8 **do**
- 5 // Update PPN hidden state $I^{i,j}$ based on the stage index;
- 6 **if** $j == 1$ **then**
- 7 $I^{i,j} \leftarrow \text{FEM}(x^{i+1})$;
- 8 **else**
- 9 $I^{i,j} \leftarrow I^{i,j-1} + M(T^{i,j-1}, x^{i,j-1})$;
- 10 **end**
- 11 // Generate the Prior $P_r^{i,j}$ from the temporal feature $T^{i,j}$ (Eq. 2);
- 12 $T^{i,j} \leftarrow \text{FEM}(I^{i,j})$;
- 13 $P_r^{i,j} \leftarrow \text{SConv}(T^{i,j})$;
- 14 // Construct DAR input feature $F_I^{i,j}$ using decoded siblings;
- 15 **if** $j == 1$ **then**
- 16 $F_I^{i,j} \leftarrow F_G^i$;
- 17 **else**
- 18 $F_{local} \leftarrow \text{FEM}(x^{i,<j})$;
- 19 $F_I^{i,j} \leftarrow \text{Concat}(F_G^i, F_{local})$;
- 20 **end**
- 21 // Predict occupancy $P_{occ}^{i,j}$ by fusing Refiner feature and Prior (Eq. 4);
- 22 $Feat \leftarrow \text{Concat}(F_I^{i,j}, P_r^{i,j})$;
- 23 $P_{occ}^{i,j} \leftarrow \sigma(\text{MLP}(\text{SConv}(Feat)))$;
- 24 // Decode occupancy $x^{i,j}$ and update context set for next stage;
- 25 Add $P_{occ}^{i,j}$ to \mathcal{P} ;
- 26 $x^{i,j} \leftarrow \text{ArithmeticDecode}(P_{occ}^{i,j})$;
- 27 $x^{i,<j+1} \leftarrow x^{i,<j} \cup x^{i,j}$;
- 28 **end**
- 29 **return** \mathcal{P} ;

pressed as follows,

$$P_o^{i,j} = \sigma(P_r^{i,j}), \quad (9)$$

$$Bit^{i,j} = Bce(P_o^{i,j}, x^{i,j}), \quad (10)$$

$$\mathcal{L} = \frac{1}{N} \sum_i \sum_j Bit^{i,j}, \quad (11)$$

where $P_o^{i,j}$ is the probability of child node occupancy estimated by PPN. N represents the number of points in the current point cloud. \mathcal{L} is the loss function used to train the PPN parameters.

Reason to use *Softplus* in M . I_1 is regarded as the feature before the sigmoid classification for the occupancy probability estimation, and T_j is considered as the correction value of the probability. If this node is occupied, the occupancy probability estimation value of the next-stage child node will increase; if this node is not occupied, the occupancy probability of the next-stage child node will decrease. Therefore, by using the *Softplus* function to convert T_j to a positive value, and then convert the occupancy codes(1 or 0) to 1 and -1, thereby better correcting the estimated occupancy probability values.

1.4. Collaboration of PPN and DAR

To present the collaboration prediction of PPN and DAR in a more detailed manner, we have presented the specific prediction process in the form of pseudo-code in Algorithm 1.

(function σ), and the loss is then calculated by performing a Binary Cross-Entropy (*Bce*) operation against the corresponding ground truth child node occupancy $x^{i,j}$ to obtain the loss for estimating the effect. The resulting loss function, \mathcal{L} , is used to optimize the PPN parameters and is ex-